ChemPubSoc Europe

DOI: 10.1002/celc.201900870

CHEMELECTROCHEM Articles

Deep Insight into Electrochemical Kinetics of Cowpea-Like Li_3VO_4@C Nanowires as High-Rate Anode Materials for Lithium-Ion Batteries

Yang Yang,[a] Min Zhao,[b] Jian Xiong,[b] Hongbo Geng,[a] Yufei Zhang,[a] Cheng Chao Li,*[a] and Jinbao Zhao*[b]

Owing to the high theoretical capacity (394 mAh g^{-1}) and appropriate lithiation voltage (0.5–1.0 V vs Li^+/Li), Li_3VO_4 is highly regarded as an attractive anode candidate for high-safety lithium-ion batteries. However, its high-rate performance is seriously restricted by the sluggish electrode kinetics. To address these problems, we synthesize cowpea-like Li_3VO_4@C nanowires through a facile electrospinning method. In this well-designed structure, Li_3VO_4 nanocrystals are uniformly encapsulated in conductive carbon nanofibers just like peas in their pods. The 1D morphology with high electronic conductivity can afford high Li^+ ions diffusion rate and fast surface charge storage mechanism, leading to significantly enhanced electrochemical kinetics. Even after 1000 cycles at 2 A g^{-1}, the reversible capacity of cowpea-like Li_3VO_4@C nanowires can be maintained at 318.0 mAh g^{-1} without obvious capacity decay.

1. Introduction

Lithium ion batteries (LIBs) have become the most dominant energy storage technology needed by the consumer electronics market since its successful commercialization released in 1990's.[1] Recently, the emerging applications of large-scale energy storage and electric vehicle industries present higher demands on LIBs in terms of energy density and safety.[2] Therefore, many new electrode materials are investigated to develop next-generation LIBs possessing higher energy density and enhanced safety.[3] According to mechanisms for lithiation processes, there are three types for anode materials can be divided: insertion type, conversion reaction type (transition metal oxides and sulfides) and alloying type (e.g., Si, Sn, Sb and Bi-based materials).[4] Nowadays, most commercial anode materials such as graphite and $Li_4Ti_5O_{12}$ are based on insertion mechanism due to the high reversibility of intercalation/deintercalation processes.

Graphite, for its theoretical specific capacity of 372 mAh g^{-1}, is the most widely used anode material.[5] But the intrinsic low lithiation voltage may lead to potential safety issues related to the formation of Li dendrites, particularly during cycling at high rates.[6] Spinel $Li_4Ti_5O_{12}$ is a high-safety insertion anode material with almost "zero strain" during cycling. However, its unsatisfactory theoretical capacity (175 mAh g^{-1}) and comparatively high lithiation voltage (~1.55 V Li^+/Li) sacrifice too much energy density when matching with cathodes.[7] In 2013, Zhou et al. reported Li_3VO_4 as a new insertion type LIB anode. The lantern-like β-Li_3VO_4 consisted of corner-shared LiO_4 and VO_4 tetrahedrons can provide empty cation active sites for Li^+ intercalation.[8] The relatively high theoretical specific capacity (394 mAh g^{-1}, based on 2 Li^+ ions insertion), appropriate lithiation voltage (mainly from 0.5 to 1.0 V vs Li^+/Li) and high Li^+ ionic mobility (10^{-4} ~ 10^{-6} S m^{-1}) render Li_3VO_4 an appropriate anode candidate. Despite multiple advantages, the poor rate capability and long cycling performance of Li_3VO_4 resulting from its low electronic conductivity hinders the practical application. Moreover, Li^+ ions diffusion in Li_3VO_4 is severely restricted by particle size and morphology.

A lot of efforts have been made to overcome these obstacles to improve the electrode kinetics of Li_3VO_4. Element doping of Na, Nb, Si, Ni, Mg and Cu into Li_3VO_4 has been demonstrated to be able to enhance the intrinsic electronic conductivity of Li_3VO_4.[9] Nonetheless, side reactions are unavoidable due to the direct contact between active materials and electrolyte. For second aspect, compositing nanostructured Li_3VO_4 with highly conductive carbon materials such as mesoporous Li_3VO_4/C hollow spheres,[10] Li_3VO_4/CMK-3 nanocomposite,[11] deflated balloon like Li_3VO_4/C/reduced graphene oxide microspheres,[12] Li_3VO_4/MWCNT composites,[13] and Li_3VO_4 nanoribbon@ graphene nanosheets nanocomposite has also been demonstrated to be favorable for ameliorating the transport of electrons and Li^+. The carbon coating on the surface of Li_3VO_4 can also serve as a protective layer to prevent the direct contact between Li_3VO_4 and the electrolyte. Among numerous nanostructures, one-dimensional (1D) nanowire structure provides direct current pathways, shorten Li^+ ion diffusion length and high surface area, which exhibits out-

[a] Y. Yang, H. Geng, Y. Zhang, Prof. C. C. Li
School of Chemical Engineering and Light Industry
Guangdong University of Technology
Guangzhou 510006, China
E-mail: licc@gdut.edu.cn
[b] M. Zhao, J. Xiong, Prof. J. Zhao
State Key Laboratory of Physical Chemistry of Solid Surfaces
College of Chemistry and Chemical Engineering
Collaborative Innovation Center of Chemistry for Energy Materials
Xiamen University, Xiamen 361005, China
E-mail: jbzhao@xmu.edu.cn

Supporting information for this article is available on the WWW under https://doi.org/10.1002/celc.201900870

standing characteristics for energy storage applications.[14] Therefore, there is reasonable to believe that fabricating 1D Li_3VO_4@C composite nanowires will greatly improve the electrochemical kinetics and structure stability during cycling.

In this work, cowpea-like Li_3VO_4@C nanowires (LVO@C NW) are prepared via a simple electrospinning method followed by the annealing process (Figure 1). In this special structure, Li_3VO_4 nanoparticles are uniformly encapsulated in the carbon nanofibers just like beans in the pods. Benefiting from the characteristic 1D nanowire morphology and uniform carbon coating layer that greatly enhances the electronic conductivity as well as shortens the transport pathways of Li^+ ions, the LVO@C NW exhibits excellent cycling stability and remarkable rate performance.

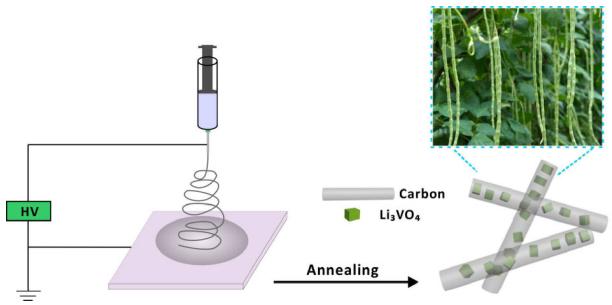

Figure 1. Schematic diagram of fabrication procedure for the LVO@C NW with a cowpea-like structure.

2. Results and Discussion

Figure 2a presents XRD patterns of the LVO@C NW and pristine LVO. All characteristic peaks of both samples match well with the standard PDF card of Li_3VO_4 (JCPDS No. 38-1247), which could be assigned to an orthorhombic crystalline structure with the Pmn21 space group. Rietveld refinement of XRD data of the LVO@C NW was also conducted, as shown in Figure 2b. The detailed crystal structure is $\alpha=\beta=\gamma=90°$, a = 6.32076 Å, b = 5.44712 Å, c = 4.95065 Å, and V = 170.451 Å^3. The results indicate that Li_3VO_4 with no impurity phase has been successfully synthesized.

Raman spectra were conducted to reveal the present of carbon in composites. For pristine LVO sample, the strongest two peaks located at 789.1 and 818.4 cm^{-1} are assigned to asymmetric stretching and symmetric stretching of VO_4^{3-}, respectively.[15] The peak at 327.1 cm^{-1} is attributed to VO_4 tetrahedron bending, and other small peaks around 200~450 cm^{-1} are related to Li–O stretching motion.[16] All corresponding peaks are agreement well with the results reported in other Li_3VO_4-based materials.[17] However, for the LVO@C NW sample, no obvious Raman peaks of Li_3VO_4 are observed. Only two broad bands located at ~1344 and 1602 cm^{-1} are detected, which are consistent with disorder D bands (defects in carbon species) and graphitic G bands (E2 g mode of sp^2 bonded graphite) of carbon.[17b,18] Because Li_3VO_4 nanocrystals are well encapsulated in carbon fiber, its Raman signal is mainly not detectable.[10] The carbon content of the composite is 24.5% measured by the thermogravimetric analysis method (Figure 2d).

To further explore the chemical environment and electronic state of the elements in the LVO@C NW, X-ray photoelectron spectra (XPS) measurements were conducted (Figure 3). The XPS spectra of C 1s (Figure 3a) can be divided into three areas,

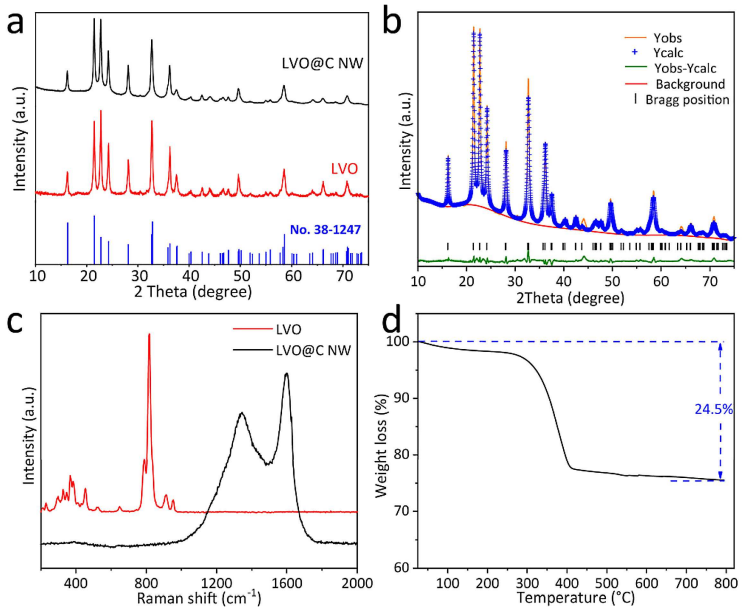

Figure 2. a) XRD patterns of the LVO@C NW and pristine LVO. b) Rietveld refinement of the LVO@C NW. c) Raman spectra of the LVO@C NW and pristine LVO. d) Thermogravimetric analysis of the LVO@C NW under flowing air.

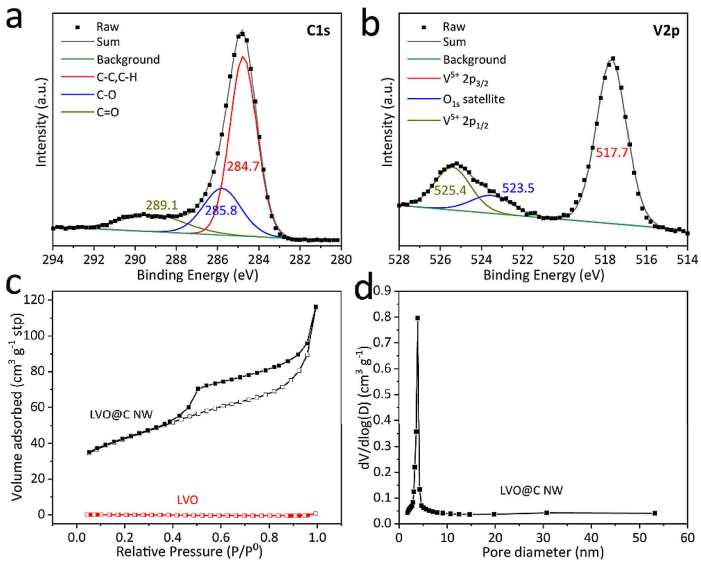

Figure 3. XPS spectra of a) C 1s and b) V 2p for the LVO@C NW. c) N_2 adsorption-desorption isotherms of the LVO@C NW and pristine LVO. d) BJH pore size distribution of the LVO@C NW.

which correspond to C–C, C–H (284.7 eV), C–O (285.6 eV) and C=O (289.1 eV), respectively. The high-resolution XPS spectra of V 2p (Figure 3b) can be deconvoluted into two dominated peaks located at 517.7 eV, and 525.4 eV, corresponding to spin-orbit V^{5+} 2p3/2 and V^{5+} 2p1/2, respectively. Another small peak at 523.5 cm^{-1} should originate from the X-ray satellite peak of O 1s.[12]

The porous properties of the LVO@C NW and pristine LVO are also investigated by N_2 adsorption-desorption isotherms (Figure 3c, 3d). The adsorption isotherm of pristine LVO is basically flat and nearly zero. Moreover, the Brunauer–Emmett–Teller (BET) specific surface area is only 0.036 $m^2 g^{-1}$, indicating the nonexistence of porous structure. In sharp contrast, the BET specific surface area of LVO@C NW is as high as 145.17 $m^2 g^{-1}$, and the adsorption isotherm is a typical type-IV curve with high porosity. The Barrett-Joyner-Halenda (BJH) pore size distribution reveals that the LVO@C NW owns a mesoporous structure centered at ~3.9 nm (pore volume of 0.16 $cm^3 g^{-1}$). High specific surface area and mesoporous architecture facilitate the full wetting of the electrolyte and reduce diffusion paths of Li^+, leading to rapid transport of Li^+.

The morphology of the LVO@C NW was studied by SEM and TEM. As shown in Figure 4a and 4b, the LVO@C NW consists of interwoven nanowires with a diameter ranging from 100 nm to 200 nm. Elemental mapping at low magnification confirms the uniform distribution of C, O and V throughout the whole region (Figure 4c). TEM images of the LVO@C NW (Figure 5a, 5b, 5c) clearly reveal the existence of outer carbon coating layer. LVO nanocrystals (average size of ~50 nm) are just like "beans", and

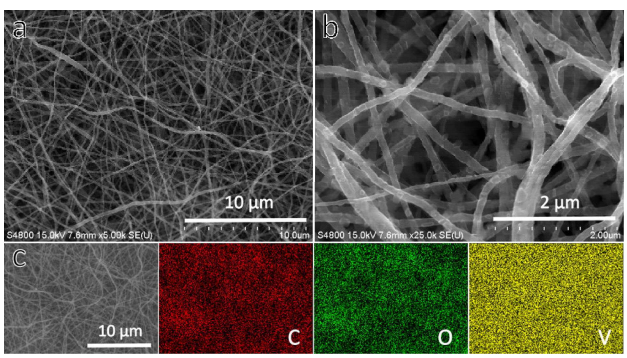

Figure 4. a, b) SEM images of the LVO@C NW. c) SEM image and elemental mapping of LVO@C NW.

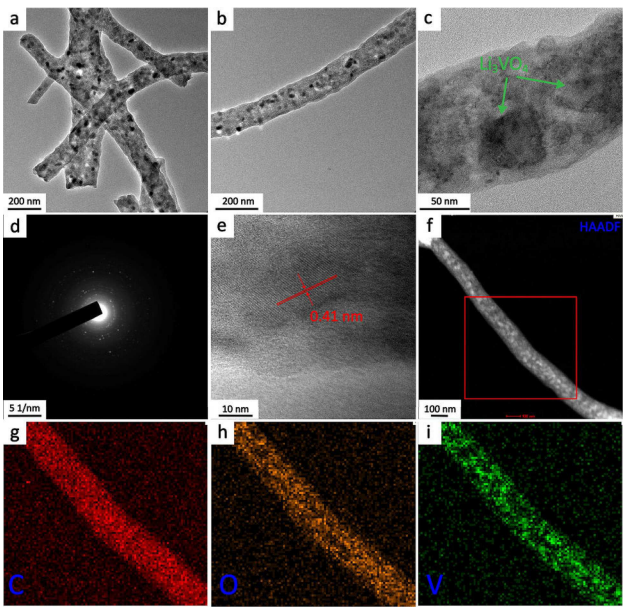

Figure 5. a–c) TEM images of the LVO@C NW. d) Selected area electron diffraction (SAED) pattern and e) HR-TEM image of the LVO@C NW. f–i) High-angle annular dark field (HAADF) image of a single LVO@C nanowire, and C, O, V elemental mapping were recorded via EDX of this region.

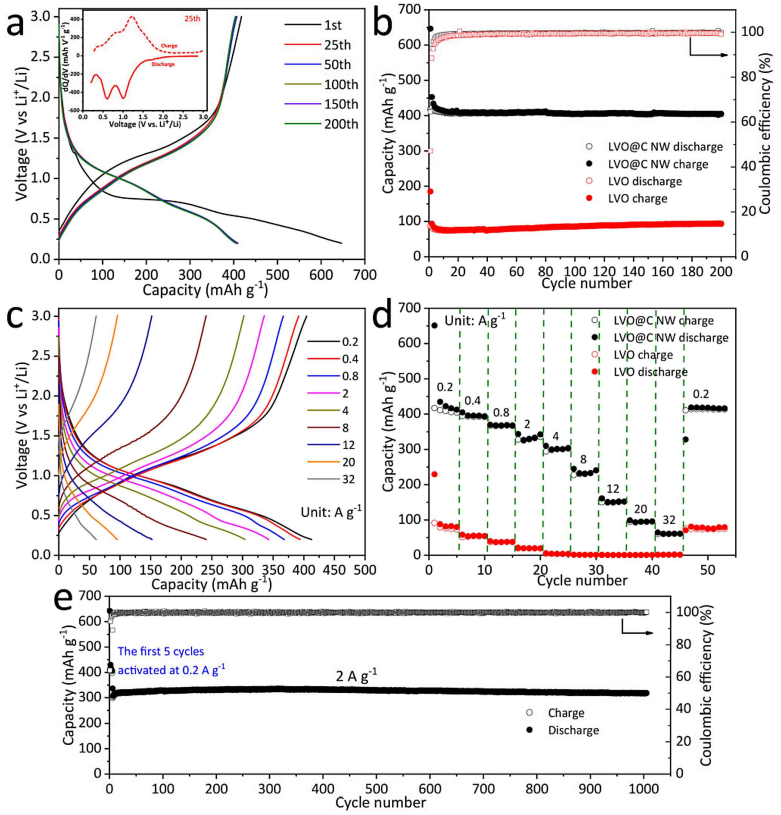

Figure 6. a) Typical voltage profiles of the LVO@C NW at 0.2 A g^{-1} (inset is the 25th cycle dQ/dV curve of the LVO@C NW). b) Cycling ability of the LVO@C NW and pristine LVO at 0.2 A g^{-1}. c) Galvanostatic discharge and charge curves and d) rate capability of the LVO@C NW from 0.2 A g^{-1} up to 32 A g^{-1}. e) High-rate capability of the LVO@C NW for 1000 cycles at 2 A g^{-1}.

amorphous carbon nanofibers are like "pods". SEM and TEM images prove that one-dimensional LVO@C nanowires with cowpea-like structural morphology have been successfully prepared. The SAED pattern of LVO@C NW (Figure 5d) exhibits concentric diffraction rings, indicating the polycrystalline structure of LVO nanocrystals. The HR-TEM image (Figure 5e) indicates that inner LVO nanocrystals with an interlayer spacing of 0.41 nm (110) are coated by the amorphous carbon layer. The uniform C, O, V elemental distribution of a single nanowire further confirms that LVO nanocrystals are well encapsulated in the carbon nanofibers.

Figure 6a shows typical voltage profiles of the LVO@C NW tested at 0.2 A g^{-1} between 0.2 and 3.0 V (vs Li^+/Li). During the initial cycle, with a coulombic efficiency (CE) of 64.6%, the discharge and charge capacities of the LVO@C NW are 646.6 and 417.7 mAh g^{-1}, respectively. The irreversible capacity loss may be attributed to the formation of solid-electrolyte-interface (SEI) on electrode surface. In subsequent cycles, the voltage profiles are basically coincident with negligible modification, implying good cycling stability. Moreover, it can be seen that most capacity contribution during the discharge process is between 0.45 and 1.25 V (the inset dQ/dV curve in Figure 6a). The appropriate voltage plateau guarantees high-safety of battery without sacrificing excessive energy density. Figure 6b show the cycling capacity of the LVO@C NW and pristine LVO at 0.2 A g^{-1}. Pristine LVO exhibits only 94.1 mAh g^{-1} after 200 cycles. In sharp contrast, a high capacity of 404.9 mAh g^{-1} is retained after 200 cycles for the LVO@C NW. Moreover, the CE is maintained above 99% after the first 5 cycles activation until the end of cycling, indicating the high reversibility of lithiation/delithiation reaction. Cycling performance of the LVO@C NW at 0.2 A g^{-1} between 0.2 and 2.0 V (vs Li^+/Li) were also investigated (Figure S2).

When both electrodes were tested at different current densities ranging from 0.2 to 32 A g^{-1}, the LVO@C NW showed impressive rate capability (Figure 2c, 2d). The LVO@C NW delivers average discharge capacities of 421.6, 397.3, 368.5, 335.3, 303.1, 236.4, 153.4, and 95.4 mAh g^{-1}, when the current density is stepwise increased from 0.2 A g^{-1} to 0.4, 0.8, 2, 4, 8, 12 and 20 A g^{-1}, respectively. Even at an extremely high current density of 32 A g^{-1}, which corresponds to an eight-second ultrafast discharge, a considerable capacity of 61.3 mAh g^{-1} can be achieved. Especially, after the current density is lowered to 0.2 A g^{-1} again, the capacity rapidly recovers to 418.6 mAh g^{-1}. On the other hand, rate performance of pristine LVO is obviously unsatisfactory, its capacity is nearly close to zero at only 4 A g^{-1}.

For LIB anodes in practical application, the long-term cycling performance is also important. After 1000 cycles at 2 A g^{-1}, the LVO@C NW also maintains a stable capacity of approximately 318.0 mAh g^{-1} with negligible capacity fading. Even at the elevated temperature of 45 °C, the LVO@C NW still

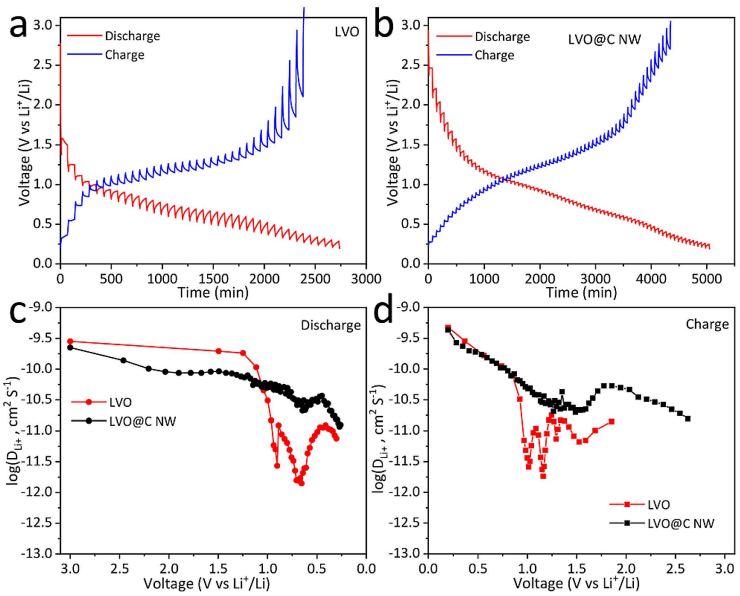

Figure 7. GITT curves of (a) pristine LVO and (b) the LVO@C NW. The calculated apparent Li^+ ions diffusion coefficients from GITT during (c) the discharge process and (d) the charge process.

exhibits a reversible capacity of 345.7 mAh g^{-1} without obvious capacity decay after 300 cycles at 2 A g^{-1} (Figure S3). The superior electrochemical performance of the LVO@C NW may be related to the characteristic cowpea-like structure, which possesses rapid transport paths of electrons and Li^+ ions during discharge-charge processes. The comparison of LVO@C NW with $Li_4Ti_5O_{12}$ and graphite in terms of gravimetric energy density, volumetric specific capacity and volumetric energy density is also shown in Figure S4 and Table S1.

To further study the chemical diffusion kinetics of Li^+ in the composites, the GITT (galvanostatic intermittent titration technology) measurement is conducted with a pulse current at 0.04 A g^{-1} for 10 min between rest intervals for 60 min (Figure 7a, 7b). Derived by Fick's second law of diffusion, the value of Li^+ diffusion coefficient is obtained by equation 1:[19]

$$D_{Li^+} = \frac{4}{\pi}\left(\frac{m_B V_m}{M_B S}\right)^2 \left[\frac{\Delta E_s}{\tau\left(\frac{dE}{d\sqrt{t}}\right)}\right]^2, \tau \ll \frac{L^2}{D_{Li^+}} \quad (1)$$

where D_{Li^+}, M_B, V_m, m_B, S, and τ denote the apparent Li^+ ions diffusion coefficient, the molecular weight, the molar volume, the mass, the geometric area of the electrode and the pulse duration, respectively, ΔE_s is the change of the equilibrium potential during a single-step GITT experiment. It can be seen a great linear relationship between E and $\sqrt{t}$ during the constant current pulse section (Figure S1b and S1d). Thus, equation 1 can be further simplified to equation 2, where ΔE_t denotes the total change of the electrode potential excluding the effect of ohmic impedance during a galvanostatic current pulse (Figure 1a, 1c).

$$D_{Li^+} = \frac{4}{\tau\pi}\left(\frac{m_B V_m}{M_B S}\right)^2 \left(\frac{\Delta E_s}{\Delta E_t}\right)^2, \tau \ll \frac{L^2}{D_{Li^+}} \quad (2)$$

Based on equation 2, D_{Li^+} of the LVO@C NW and pristine LVO are plotted in Figure 7c and 7d. Both samples exhibit similar trends in the variation of D_{Li^+} as a function of electrode potential. Moreover, D_{Li^+} of both samples show a slight local minimum at 0.5 ~ 1.0 V (discharge process) and 1.0 ~ 1.75 V (charge process), which is related to the voltage plateau (inset in Figure 6a). This phenomenon is likely due to the formation of a new phase in this voltage region.[13,20] The two-phase transition domain may increase the interaction between Li^+ ions and host material, leading to lower diffusion rate, which is similar to other insertion-type electrode materials.[21] The lithium diffusion in LVO@C NW is clearly faster than that of pristine LVO over the major intercalation/deintercalation processes.

To get more insight into the prominent high-rate performance of the LVO@C NW, CV experiments at various scan rate ranging from 0.2 to 2 mV s^{-1} have been carried out to investigate the charge storage mechanism (Figure 8). The cathodic peak currents (i_p) of pristine LVO (Figure 8a) and the LVO@C NW (Figure 8c) become larger and shift to more positive position with the increase of scan rates (υ). However, the LVO@C NW exhibits much lower polarization obviously. Generally, there is an empirical relationship between i_p and υ as follows equation 3:[22]

$$i_p = a\upsilon^b \quad (3)$$

where a and b are changeable factors. And the value of b can be estimated by doing linear fitting plots of lg (i_p) vs. lg (υ). A electrochemical process with b value of 0.5 reveals that the Li^+ storage is completely controlled by semi-infinite diffusion,

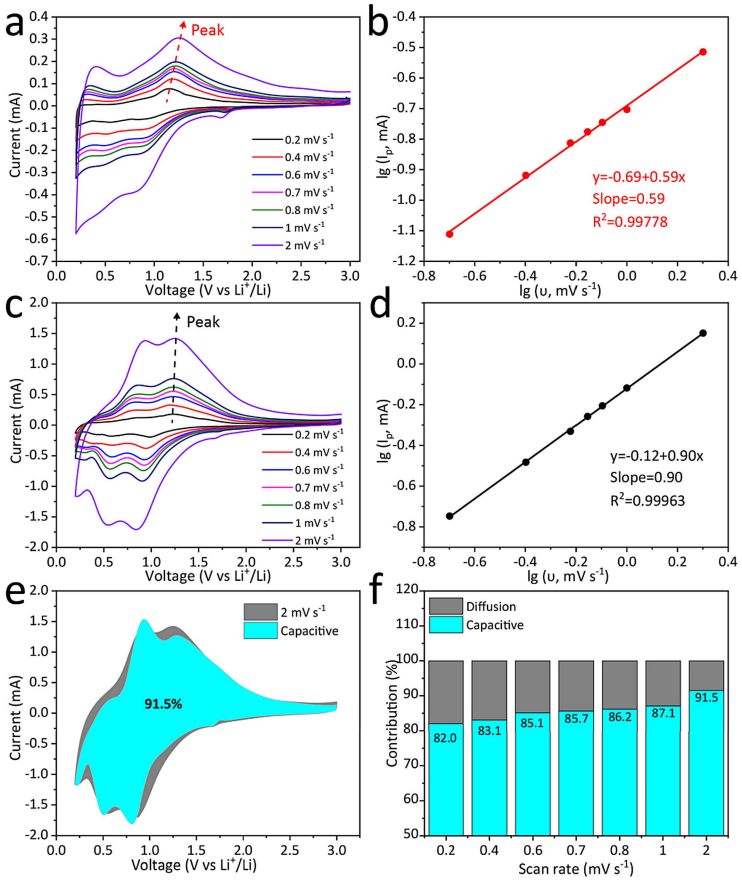

Figure 8. a) CV curves at different scan rates and b) the relationship between cathodic peak current i_p and scan rate υ of pristine LVO. c) CV curves at different scan rates and d) the relationship between cathodic peak current i_p and scan rate υ of the LVO@C NW. e) CV curves at 2 mV s^{-1} showing the capacitive contribution (cyan region) to the total current. f) Percentages of capacitive contributions of the LVO@C NW at different scan rates.

whereas $b = 1.0$ represents a capacitive process.[23] The calculated *b*-value of the LVO@C NW is 0.90 (Figure 8d), which is much larger than that of pristine LVO (0.59, Figure 8b). The larger *b*-value implies that electrochemical reactions of the LVO@C NW tends to be controlled by the fast near-surface capacitive behavior. The percentages of capacitive contribution can be further quantified according to equation 4 as follows:

$$i = k_1\upsilon + k_2\upsilon^{1/2} \quad (4)$$

in which $k_1\upsilon$ and $k_2\upsilon^{1/2}$ represent the capacitive contribution and diffusion-controlled contribution, respectively. Percentages of capacitive contributions of the LVO@C NW at different scan rates are summarized in Figure 8f. With the increase of scan rates (from 0.2 to 2.0 mV s^{-1}), the percentage of capacitive contributions goes up gradually from 82.0% to 91.5% (Figure 8e illustrates the capacitive current (cyan region) compared to the total current). The high capacitive contribution is in favor of high-rate capability.

To understand the synergetic effects of high Li^+ ions diffusion rate and rapid surface charge storage behavior of the LVO@C NW, EIS (electrochemical impedance spectroscopy) measurements were performed after 20 cycles (Figure S5). Both plots display one compressed semicircle and one inclined line. The inset equivalent circuit was used to fit the EIS parameters. The compressed semicircle is composed of two semicircles, represents SEI resistance (R_1) and charge-transfer resistance (R_2), respectively. And the inclined line is related to the Warburg impedance (W_o).[24] Obviously, both R_1 (30.5 Ω) and R_2 (14.4 Ω) of the LVO@C NW are smaller than those of pristine LVO (37.6 Ω and 41.6 Ω, respectively), suggesting the enhanced charge-transfer and charge-transport capability.

From a structural point of view, the cowpea-like structure of the LVO@C NW shows three outstanding features (Figure 9): (1) The interwoven carbon nanofibers form a conductive integrity and act as highways for the transport of electrons. (2) The 1D morphology and abundant mesoporous efficaciously improve the contact between electrode material and electrolyte. (3) Nano-sized LVO nanocrystals encapsulated in the carbon nanofibers can reduce diffusion paths of Li^+ ions. Due to the rational structural design, the LVO@C NW possesses fast surface-controlled electrochemical kinetics, which corroborate the higher apparent Li^+ diffusion coefficient and much reduced charge-transfer resistance.

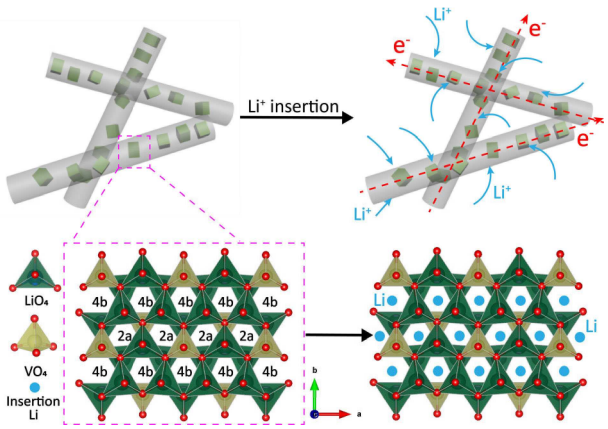

Figure 9. Schematic illustration of the structural advantages and Li^+ insertion mechanism of the LVO@C NW.

3. Conclusions

In summary, cowpea-like Li_3VO_4@C nanowires (LVO@C NW) are successfully prepared via a simple electrospinning method, followed by annealing in Ar atmosphere. The cowpea-like structure is able to not only increase the contact area and wetting effect between material and electrolyte, and reduce diffusion paths of Li^+, but also accelerate the transfer of electrons, thereby causing higher apparent Li^+ diffusion coefficient and faster surface charge storage mechanism. Owing to the significantly improved electrochemical kinetics, the as-prepared LVO@C NW exhibited remarkable rate capability (considerable capacity of 61.3 mAh g^{-1} at a super high current density of 32 A g^{-1}) and excellent long-term cycling performance (1000 stable cycles at 2 A g^{-1} without obvious capacity decay). This work demonstrated the feasibility and practicality of adopting the LVO@C NW as high-rate anode materials for lithium-ion batteries.

Experimental Section

Fabrication of the LVO@C NW

0.173 g V_2O_5 (Shanghai Chemical Reagent 3rd Factory) and 0.211 g Li_2CO_3 (Sinopharm Chemical Reagent Co., Ltd.) were added in 10 mL H_2O with magnetic stirring at 25 °C. Next, 0.4 g polyvinyl alcohol (PVA-124, Xilong Scientific Co., Ltd.) and 0.013 g sodium dodecyl sulfate (SDS, Shanghai Aladdin Biochemical Technology Co., Ltd.) were added in the above orange solution. Then it is stirred for 60 mins at 85 °C, the final electrospinning solution is obtained. The as-prepared electrospinning solution was loaded into a 5 mL plastic syringe with a stainless-steel nozzle (0.25 mm inner diameter). A 15 kV voltage was applied between the collector (a piece of aluminum foil) and nozzle with the distance of 20 cm, and the feeding rate was controlled at 0.03 mL min^{-1}. As-spun nanofibers were collected and annealed under Ar atmosphere for 10 h at 600 °C to obtain the LVO@C NW. Pristine Li_3VO_4 was prepared by a conventional solid-state method.[8] Typically, 0.173 g V_2O_5 and 0.211 g Li_2CO_3 were mixed using the mortar, and annealed in the muffle furnace for 6 h at 600 °C. Then the powder was ground and further annealed in the muffle furnace for 3 h at 900 °C.

Materials' Characterization

The morphologies of LVO@C NW were investigated using scanning electron microscopy (Hitachi, S-4800) and transmission electron microscopy (JEOL, JEM-2100). The phases of the samples were identified by Powder X-ray diffraction (XRD, Miniflex 600, Rigaku). Raman spectra were recorded using a Laser Confocal Raman Microspectrometer (inVia, Renishaw) with a 532 nm wavelength laser excitation source. X-ray photoelectron spectroscopy (XPS) measurements were conducted on PHI Quantum 2000. The specific surface area and porosity of the samples were investigated using a porosity instrument (ASAP 2020, Micromeritics). Thermogravimetric analysis (TGA) was attained on SDT Q600 (TA instruments) system from 25 °C to 800 °C under air atmosphere.

Electrochemical Measurements

Electrochemical properties were evaluated by using CR2016-type coin cells assembled in an Ar-filled glovebox. For the fabrication of working electrode, a homogenized mixture of LVO@C NW, acetylene black, and polyvinylidene fluoride (PVDF) binder (in weight ratio of 7:2:1) in N-methylpyrrolidine (NMP) solvent was coated onto the Cu foil and dried overnight at 80 °C in the vacuum oven. The typical loading mass of active materials in working electrodes was 0.8 ~ 1.1 mg cm^{-2}. 1 M $LiPF_6$ in ethylene carbonate and diethyl carbonate (EC-DEC, 1:1 v/v) as the electrolyte, and Celgard 2400 as the separator. The LAND battery tester was adopted for galvanostatic charging/discharging tests at 0.2 ~ 3.0 V vs Li^+/Li. Cyclic voltammetry (CV) was measured in electrochemical workstation (Autolab 302 N, Metrohm) at various scan rates. Electrochemical impedance spectra (EIS) was measured in the frequency from 100 mHz to 100 kHz by using a Solartron 1260 A impedance/gain-phase analyzer coupled with Solartron analytical 1287 A potentiostat/galvanostat.

Acknowledgements

Prof. Cheng Chao Li would like to thank the support by National Natural Science Foundation of China (No. 51771058) and Guangdong Province Universities and Colleges Pearl River Scholar Funded Scheme.

Conflict of Interest

The authors declare no conflict of interest.

Keywords: lithium-ion batteries · anode materials · Li_3VO_4 · nanowires · electrospinning

[1] J. M. Tarascon, M. Armand, *Nature* **2001**, *414*, 359–367.
[2] V. Etacheri, R. Marom, R. Elazari, G. Salitra, D. Aurbach, *Energy Environ. Sci.* **2011**, *4*, 3243–3262.
[3] a) S. Ni, J. Zhang, X. Lv, X. Yang, L. Zhang, *J. Power Sources* **2015**, *291*, 95–101; b) Z. J. Yao, X. H. Xia, Y. Zhang, D. Xie, C. Z. Ai, S. W. Lin, Y. D. Wang, S. J. Deng, S. H. Shen, X. L. Wang, Y. Yu, J. P. Tu, *Nano Energy* **2018**, *54*, 304–312; c) Z. J. Yao, X. H. Xia, D. Xie, Y. D. Wang, C. A. Zhou, S. F. Liu, S. J. Deng, X. L. Wang, J. P. Tu, *Adv. Funct. Mater.* **2018**, *28*, 8.
[4] a) M. N. Obrovac, V. L. Chevrier, *Chem. Rev.* **2014**, *114*, 11444–11502; b) M. V. Reddy, G. V. S. Rao, B. V. R. Chowdari, *Chem. Rev.* **2013**, *113*, 5364–5457.

[5] F. Schipper, D. Aurbach, *Russ. J. Electrochem.* **2016**, *52*, 1095–1121.
[6] C. K. Zhang, H. Q. Song, C. F. Liu, Y. G. Liu, C. P. Zhang, X. H. Nan, G. Z. Cao, *Adv. Funct. Mater.* **2015**, *25*, 3497–3504.
[7] L. Shen, S. Chen, J. Maier, Y. Yu, *Adv. Mater.* 1701571.
[8] Y. Yang, J. Li, D. Chen, J. Zhao, *J. Electrochem. Soc.* **2017**, *164*, A6001–A6006.
[9] a) J. Zhou, B. Zhao, J. Song, B. Chen, X. Ma, J. Dai, X. Zhu, Y. Sun, *Solid State Ionics* **2018**, *322*, 30–38; b) L. Zhao, H. Duan, Y. Zhao, Q. Kuang, Q. Fan, L. Chen, Y. Dong, *J. Power Sources* **2018**, *378*, 618–627; c) K. Wang, H. Fu, Z. Li, M. Xia, X. Liang, R. Qi, G. Cao, X. Lu, *ChemElectroChem* **2018**, *5*, 478–482; d) C. Liao, Y. Wen, Z. Xia, R. Qin, X. Liu, Y. Yu, B. Shan, T. Zhai, H. Li, *Adv. Energy Mater.* **2018**, *8*; e) C. Zhang, K. Wang, C. Liu, X. Nan, H. Fu, W. Ma, Z. Li, G. Cao, *NPG Asia Mater.* **2016**, *8*, e287; f) Y. Dong, Y. Zhao, H. Duan, P. Singh, Q. Kuang, H. Peng, *J. Power Sources* **2016**, *319*, 104–110.
[10] Y. Yang, J. Li, X. He, J. Wang, D. Sun, J. Zhao, *J. Mater. Chem. A* **2016**, *4*, 7165–7168.
[11] X. Xu, F. Niu, D. Zhang, C. Chu, C. Wang, J. Yang, Y. Qian, *J. Power Sources* **2018**, *384*, 240–248.
[12] H. Liu, P. Hu, Q. Yu, Z. Liu, T. Zhu, W. Luo, L. Zhou, L. Mai, *ACS Appl. Mater. Interfaces* **2018**, *10*, 23938–23944.
[13] E. Iwama, N. Kawabata, N. Nishio, K. Kisu, J. Miyamoto, W. Naoi, P. Rozier, P. Simon, K. Naoi, *ACS Nano* **2016**, *10*, 5398–5404.
[14] a) L. Mai, X. Tian, X. Xu, L. Chang, L. Xu, *Chem. Rev.* **2014**, *114*, 11828–11862; b) L. Mai, X. Xu, L. Xu, C. Han, Y. Luo, *J. Mater. Res.* **2011**, *26*, 2175–2185.
[15] a) J. Liu, P.-J. Lu, S. Liang, J. Liu, W. Wang, M. Lei, S. Tang, Q. Yang, *Nano Energy* **2015**, *12*, 709–724; b) G. Yang, B. W. Zhang, J. Y. Feng, Y. Lu, Z. Q. Wang, V. Aravindan, M. Aravind, J. L. Liu, M. Srinivasan, Z. X. Shen, Y. Z. Huang, *J. Mater. Chem. A* **2018**, *6*, 456–463.
[16] D. J. Kim, B. E. Jun, C.-S. Kim, H. K. Kim, J. N. Kim, Y.-H. Hwang, *J. Appl. Phys.* **2003**, *93*, 1697–1700.
[17] a) Y. Shi, J.-Z. Wang, S.-L. Chou, D. Wexler, H.-J. Li, K. Ozawa, H.-K. Liu, Y.-P. Wu, *Nano Lett.* **2013**, *13*, 4715–4720; b) Q. Li, J. Sheng, Q. Wei, Q. An, X. Wei, P. Zhang, L. Mai, *Nanoscale* **2014**, *6*, 11072–11077; c) Z. Jian, M. Zheng, Y. Liang, X. Zhang, S. Gheytani, Y. Lan, Y. Shi, Y. Yao, *Chem. Commun.* **2015**, *51*, 229–231.
[18] A. C. Ferrari, J. Robertson, *Phys. Rev. B* **2000**, *61*, 14095–14107.
[19] J. S. Hong, J. R. Selman, *J. Electrochem. Soc.* **2000**, *147*, 3190–3194.
[20] P. Rozier, E. Iwama, N. Nishio, K. Baba, K. Matsumura, K. Kisu, J. Miyamoto, W. Naoi, Y. Orikasa, P. Simon, K. Naoi, *Chem. Mater.* **2018**, *30*, 4926–4934.
[21] a) J. Sheng, H. Zang, C. Tang, Q. An, Q. Wei, G. Zhang, L. Chen, C. Peng, L. Mai, *Nano Energy* **2016**, *24*, 130–138; b) Q. Wang, B. Zhao, S. Zhang, X. Gao, C. Deng, *J. Mater. Chem. A* **2015**, *3*, 7732–7740; c) K. J. Griffith, K. M. Wiaderek, G. Cibin, L. E. Marbella, C. P. Grey, *Nature* **2018**, *559*, 556-++.
[22] P. Simon, Y. Gogotsi, B. Dunn, *Science* **2014**, *343*, 1210–1211.
[23] J. Liu, J. Wang, C. Xu, H. Jiang, C. Li, L. Zhang, J. Lin, Z. X. Shen, **2018**, *5*, 1700322.
[24] a) Y. Shi, J. Gao, H. D. Abruna, H.-J. Li, H.-K. Liu, D. Wexler, J.-Z. Wang, Y. Wu, *Chem. Eur. J.* **2014**, *20*, 5608–5612; b) S. Hu, Y. F. Song, S. Y. Yuan, H. M. Liu, Q. J. Xu, Y. G. Wang, C. X. Wang, Y. Y. Xia, *J. Power Sources* **2016**, *303*, 333–339.

Manuscript received: May 24, 2019
Revised manuscript received: June 23, 2019
Accepted manuscript online: June 26, 2019